Electronic
Research Archive

https://www.aimspress.com/journal/ERA

ERA, 33(11): 6652–6671.
DOI: 10.3934/era.2025294
Received: 08 July 2025
Revised: 23 September 2025
Accepted: 04 November 2025
Published: 13 November 2025

Research article

Exploring of new biomarkers for early diagnosis of Alzheimer's disease based on a large scale neurovascular coupling model

Ruoyao Xu, Youjun Liu, Bao Li, Tongna Wang, Yuejuan Xu and Liyuan Zhang*

Department of Biomedical Engineering, Beijing University of Technology, Beijing 100124, China

* **Correspondence:** Email: LiyuanZhang@bjut.edu.cn.

Abstract: Alzheimer's disease (AD) is an age-related neurodegenerative disorder that is difficult to diagnose early. Traditional methods can only confirm the diagnosis when symptoms are evident, but by that time, brain damage is irreversible. Recent research has found that changes in brain activity patterns occur early in AD. Using brain imaging and computational modeling techniques, we can hopefully detect these changes before the onset of symptoms, enabling early intervention. In this paper, we constructed a neurovascular coupling (NVC) whole-brain dynamic model by integrating brain structural data with biophysical modeling methods, aiming to explore the association between dynamical parameters and biomarkers of AD and to reveal their relationship with the overall brain function and network dynamic changes. First, the model simulates properly the resting-state functional connectivity (FC) at various stages of AD development; second, the strength of circulatory connectivity and NVC parameters generated by the brain simulation may be some potential new indicators for the early diagnosis of AD; and finally, the predictive ability of the indicator is quantified using the area under the curve (AUC) values of the receiver operating characteristic (ROC) curves, which suggests a dual strategy for the early diagnosis of biomarkers. These new indicators not only deepen our understanding of the mechanisms of disease progression but also provide an important theoretical basis and technical support for the formulation of early intervention strategies and the development of novel therapeutic approaches.

Keywords: Alzheimer's disease; early diagnosis; multimodal data; neurovascular coupling; whole brain model

---

1. Introduction

The pathogenesis of Alzheimer’s disease (AD) is closely related to a dysfunction of the neurovascular coupling (NVC), a key mechanism for maintaining brain function and safeguarding energy metabolism by coordinating neuronal activity with cerebral blood flow supply [1]. When the NVC is impaired, cerebral blood flow regulation decreases, leading to neuronal hypoxia and metabolic waste accumulation, accelerating β-amyloid deposition and tau protein phosphorylation. Studies have shown that NVC abnormalities often appear earlier than typical pathologic markers, which provides an important window for early diagnosis [2,3]. However, existing clinical testing techniques rely mainly on advanced structural lesions or molecular imaging features, which make it difficult to capture early functional NVC changes, resulting in patients missing the optimal intervention period when diagnosis is made.

Current AD research models have obvious limitations. Although transgenic animal models can simulate some of the pathological features, they are unable to fully reproduce the dynamic dysregulation of NVC in humans, especially the key mechanisms such as impaired perivascular gap drainage and desynchronization of neural electrical activity [4]. Computational models, on the other hand, are limited by the simplified treatment of cross-scale physiological coupling, making it difficult to quantify the degree of NVC attenuation in different disease courses [5]. This lack of mechanism elucidation directly contributes to the poor specificity of diagnostic markers; the misdiagnosis rate is as high as 30%–40% [6] in the mild cognitive impairment stage. The development of multimodal dynamic models incorporating bi-directional neurovascular regulatory mechanisms will be an important way to break through the bottleneck of early diagnosis.

In this study, we constructed a computational model of NVC integrating multimodal data, and established a whole-brain model of AD containing N-methyl-D-aspartic acid (NMDA)/Gamma-aminobutyric acid (GABA) neuronal dynamics by integrating the diffusion tensor imaging (DTI) structural connectivity network and the functional features of 68 brain regions. The model not only reveals the dynamic evolution of NVC mechanisms at different stages of AD but also quantitatively analyzes the association mechanism between novel biomarkers such as amplitude of low frequency fluctuation (ALFF)/cerebral blood flow (CBF) ratio and Aβ/p-tau pathology. Based on the simulation results, we propose a dual detection strategy with clinical translational value, confirming the critical value of NVC efficiency in the early diagnosis of AD. This study provides an innovative computational model paradigm for breaking the bottleneck of AD early diagnosis and establishes a reliable simulation evaluation platform for the optimization of clinical intervention strategies.

2. Methods

2.1. Data source and type

ADNI database: The Alzheimer’s Disease Neuroimaging Initiative (ADNI) database provided the data used in this study, which was launched in 2003 to monitor the progression of mild cognitive impairment (MCI) and early Alzheimer’s disease using a combination of magnetic resonance imaging (MRI), positron emission tomography (PET), other biomarkers, and neuropsychological testing. ADNI was approved by the regional ethical review boards of all the participating institutions. Regional ethical review boards of the participating institutions and all subjects provided written informed consent in accordance with the Declaration of Helsinki [7].

In order to improve the sensitivity of the new index, people with early mild cognitive impairment (EMCI) were selected to look for differences between normal people and this population in the subgroup of mild cognitive impairment. The study included 136 participants with ADNI around the age of 80 who had undergone resting-state functional magnetic resonance imaging (rs-fMRI), DTI, MRI (T1w), and PET, and were categorized into the Cognitive Normal Cohort (CN), the EMCI group, and the AD group. Of the 136 participants, 18 had no matched data, which did not fulfill the criteria for Aβ positivity on Aβ PET (SUVR > 1.11) [8–10] and Tau positivity on Tau PET. We excluded the above populations from the study. Finally, a total of 118 ADNI participants were included in the cross-sectional study, including 42 CNs, 38 EMCIs, and 38 ADs. Data selection criteria: http://adni.loni.usc.edu/methods/documents.

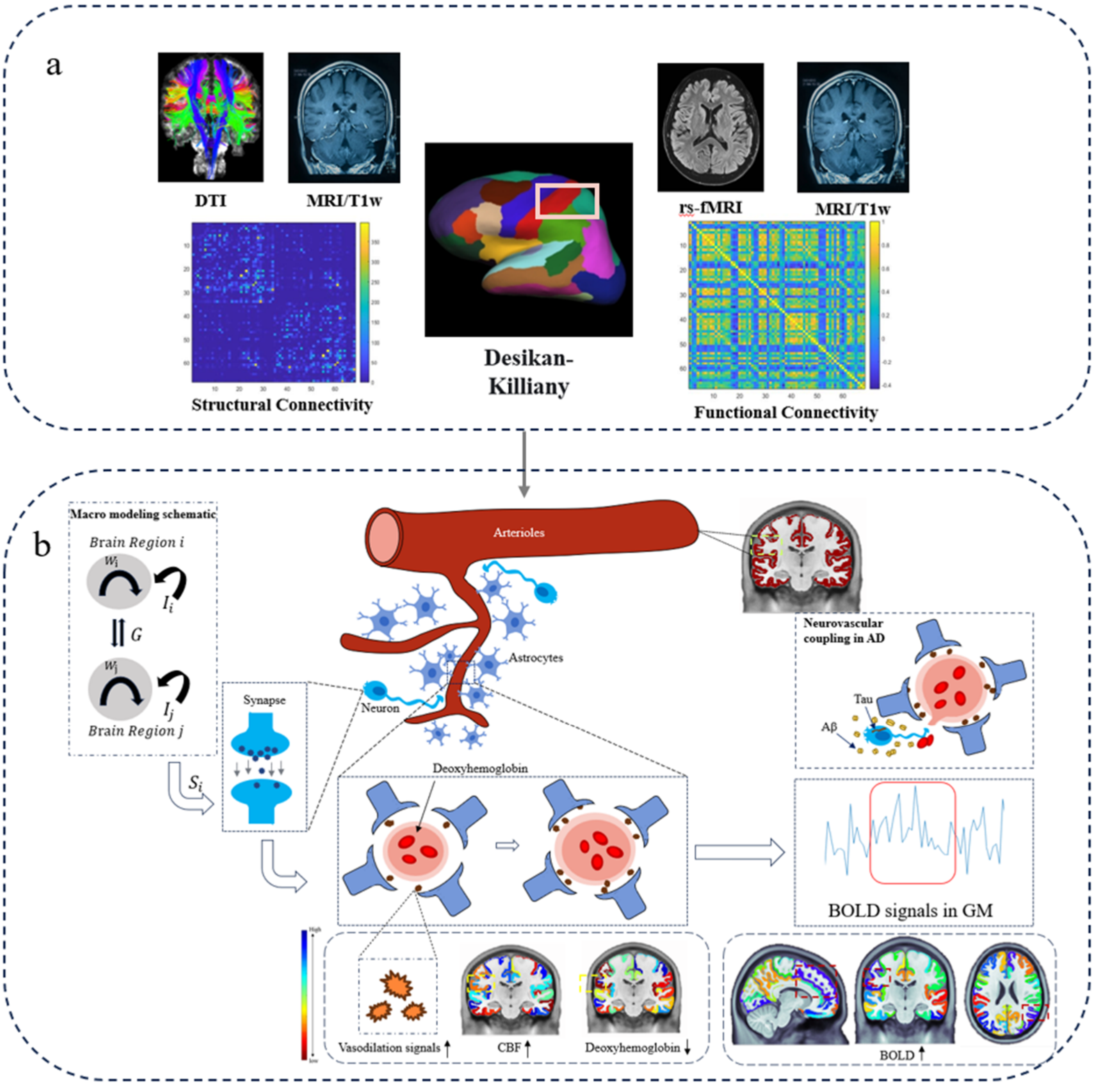

Figure 1. (a) The entire macro process. Specifically, FC was generated by fMRI and MRI T1w under the Desikan-Killiany template, and SC was generated by DTI and MRI T1w under the Desikan-Killiany template. (b) Specific micro-modeling process. Specifically, we reflected the process of neurovascular coupling in the model creation process, as well as the parameter indicators generated in the process.

2.2. Data preprocessing

DTI uses DSI-Studio to preprocess and extract the structural connectivity (SC) matrix [11–13]. The Desikan-Killiany template was set as the basis for the delineation of brain regions, and the fibers of the brain were traced to generate corresponding fiber connections in the regions of interest, which in turn generated a matrix of structural connections.

Preprocessing of rs-fMRI and T1: The steps for preprocessing functional magnetic resonance imaging (rs-fMRI) and T1-weighted images using the RestPlus toolbox included [14] format conversion, removal of time points, temporal layer correction, motion correction, alignment, and normalization. Using the DPABI toolbox, the Desikan-Killiany template was selected as the basis for brain region delineation, the functional connectivity (FC) between each pair of brain regions was calculated, and a 68 × 68 correlation matrix was generated. This section corresponds to Figure 1a, which shows the process of generating FC and SC.

All the above software was run using Windows and MATLAB version 2021a.

The PET processing software uses POMD software to extract the standard uptake value ratio (SUVR) [15]. SUV represents the radioactive concentration of the lesion (kBq/mL)/injection dose (MBq)/body weight (kg). SUVR represents the average standardized uptake value (SUV) of ROI/average SUV of reference region. The key point is to input the DK template we use, extract the average value of each brain region, and perform subsequent calculations.

2.3. NVC computational modeling of whole-brain resting-state dynamics

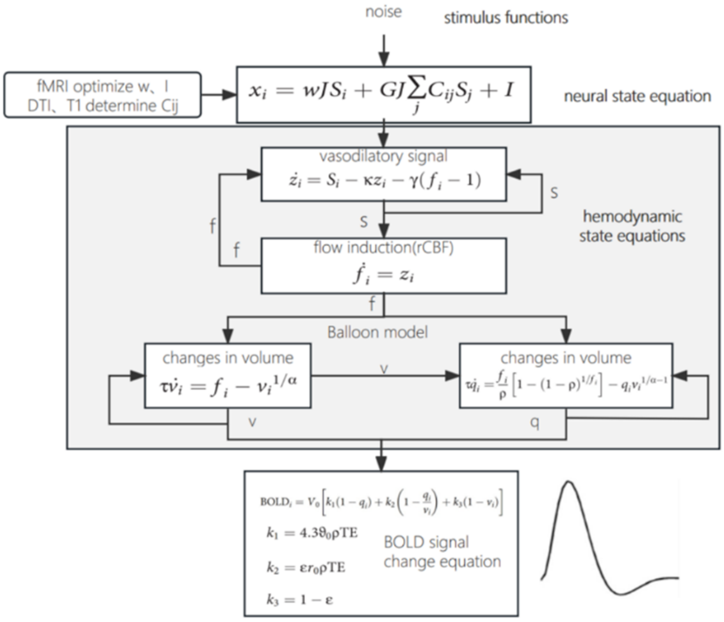

Figure 2. Workflow of the NVC modeling. By setting up a neuronal noise-driven model, DTI generates a SC matrix that provides the parameter C_{ij}, x_i denotes the input from each brain region, and the mean-field model yields synaptic activity S_i, which causes a change in the vasodilatory signal z_i, which affects the blood flow hair, which in turn changes the vascular volume v_i and the deoxyhemoglobin content q_i, and ultimately yields the BOLD signal, which is the simulated FC.

Brain structural data were combined with brain computational modeling to simulate parameters related to neural activity, blood flow, and blood oxygen level–dependent (BOLD) signal to identify Alzheimer's patients, mild cognitive impairment, and the normal population. We developed a mean-field model to simulate resting-state neural activity, where synaptic activity changes drive a balloon model to generate deoxyhemoglobin dynamics and ultimately produce BOLD signals for biomarker discovery and predictive analysis. The specific process is illustrated in Figure 2. This section corresponds to Figure 1b and is a formulaic representation of the microscopic mechanism.

2.3.1. Mean-field model

Mean-field modeling (MFM), based on a combination of real neuronal and synaptic dynamics, restores neuronal activity at the microscopic level [16]. Using the Desikan-Killiany brain atlas, the brain surface was divided into 68 regions, and different physical parameters (e.g., excitatory subcortical inputs I and intra-regional circulatory connections w) were assigned to each region (see Eq (2.1)), as the strength of connections and inputs differed between cortical regions. MFM modeled the neurodynamics of the 68 regions of interest (ROIs), which were determined by four main factors: i) intra-regional connections (w), ii) inter-regional inputs, iii) excitatory subcortical inputs (I), and iv) neural noise. w denotes the strength of intra-regional connections, with higher inter-regional inputs being stronger, and the strength of the connections is determined by the SC and a global constant, G; I represents the excitatory subcortical inputs (in nanoamps), which reflect the superposition of excitatory and inhibitory neural activity. The noise is assumed to be Gaussian with amplitude σ.

The mean-field model can be derived using a set of nonlinear stochastic differential equations:

$$\begin{gathered} \dot{S_i} = -\frac{S_i}{\tau_s} + r(1 - S_i)H(x_i) + \sigma v_i(t) \\ H(x_i) = \frac{ax_i - b}{1 - \exp\left(-d(ax_i - b)\right)} \\ x_i = wJS_i + GJ\sum_j C_{ij}S_j + I \end{gathered} \tag{2.1}$$

In this model, x_i denotes the input current to the region, $H(x_i)$ denotes the overall firing rate of the region, and S_i denotes the average synaptic gating variable in region *i*. The input stream is determined by the cyclic connection strength w, the excitatory subcortical input *I*, and the interregional information flow that controls the strength of the information flow between the two cortical regions corresponding to the SC between cortical regions *i* and j. *G* is the global coupling, and the value of the synaptic coupling *J* was set to 0.2609 Na according to literature reference values [17]. Values of the parameters have been set to a = 270 N/C, b = 108 Hz, and d = 0.154 s. The dynamical parameter of synaptic activity was set to r = 0.641 and τ_s = 0.1 s, corresponding to the non-correlated normal Gaussian noise with noise amplitude controlled by σ.

2.3.2. Windkessel-Balloon modeling

The simulated neural activity S_i was fed into the Balloon-Windkessel ischemic model [18] to predict the fMRI signal at each ROI. That is, synaptic activity S_i allows for an increase in the vasodilator signaling pathway z_i. Blood flow f_i, accompanied by changes in blood volume v_i and deoxyhaemoglobin content q_i, is proportional to this signal. The equations related to these biological processes are as follows:

$$\dot{z_i} = S_i - \kappa z_i - \gamma(f_i - 1)$$

$$\dot{f_i} = z_i$$

$$\tau \dot{v_i} = f_i - {v_i}^{1/\alpha}$$

$$\tau \dot{q_i} = \frac{f_i}{\rho}[1 - (1 - p)^{1/f_i}] - q_i {v_i}^{1/\alpha - 1} \tag{2.2}$$

In which resting oxygen extraction fraction ρ = 0.34, signal decay rate κ = 0.65s^{-1}, elimination rate γ = 0.41s^{-1}, hemodynamic transfer time τ = 0.98 s, and Grubb's index α = 0.32. Given q_i and v_i, the BOLD signal is as follows [19–21]:

$$BOLD_i = V_0[k_1(1 - q_i) + k_2(1 - \frac{q_i}{v_i}) + k_3(1 - v_i)] \tag{2.3}$$

The V_0 = 0.02 is the resting blood volume fraction, (k_1, k_2, k_3) is a number of magnetic field strength–dependent parameters and some acquisition dependent parameters. The values are given by the following equation [20]:

$$k_1 = 4.3\vartheta_0 \rho TE$$

$$k_2 = \varepsilon r_0 \rho TE$$

$$k_3 = 1 - \varepsilon \tag{2.4}$$

The parameter ϑ_0 = 28.265, and B_0 is the frequency offset with respect to the strength of the main magnetic field of the outer surface of the magnetized vessel. B_0 = 3T in the ADNI dataset, the intravascular relaxation rate is r_0 = 110 Hz, the ratio of the intravascular to extravascular MR signals is e = 0.47 [20], and the echo time in the dataset is TE = 30.0 ms; all are observed at a magnetic field strength of 3T. This section corresponds to Figure 1b and is key to the connection between each step of the micro-mechanism.

2.4. Parameter estimation for the NVC model

In the original model, the circulating connection strength w and the excitatory subcortical input I were considered identical in all regions. In this study, the model was relaxed in such a way that each region had its own cyclic connection strength w and its own excitatory subcortical input I. We call the model a relaxed dynamical mean-field model (rMFM).

By maximizing the proximity between simulated FC and empirical FC in the training set, we optimized 138 rMFM parameters, corresponding to w_i, I_i, the global scaling factor G, and the noise factor σ. These 138 parameters correspond to each individual. A previously developed algorithm for inversion of MEG neural quality models was used for this optimization [22], which was based on the expectation used in the DCM [21] maximization algorithm. The algorithm can be briefly described as follows.

First, the initial parameters were log-transformed to ensure their positive values. Then, the FC matrix was simulated, and the residuals were computed using the finite difference method to obtain the Jacobi matrix. Next, the error covariance matrix was initialized, and the error covariance matrix [21] and model parameters were updated through iterations until convergence. The process involves calculating the residuals using empirical and simulated data and updating the parameters until the optimization converges. Finally, the optimal model parameters are selected through multiple stochastic initializations and iterative optimization to maximize the Pearson correlation between the simulated and empirical FCs.

We divided all subjects into a discovery set and a validation set. All parameter optimization was performed exclusively on the discovery set (e.g., a subset of subjects from the CN and AD groups). The optimized parameter model was then directly applied to the validation set (the remaining subjects), which had not participated in the optimization process, to compute correlations between simulated FC and empirical FC. The persistence of significant correlations in the validation set provides crucial evidence for the model's generalization capability. Our parameter optimization is not entirely unconstrained. By setting initial parameter values within biologically plausible ranges and strictly constraining their variation during optimization (e.g., all parameters > 0), we effectively impose a box constraint—an implicit form of regularization. This prevents parameters from drifting into unrealistic domains, thereby mitigating overfitting risks.

2.5. Extraction of SUVR for Aβ and Tau proteins in PET images

In positron emission tomography (PET) image analysis, the standardized uptake value ratio (SUVR) is used to assess and compare the relative amounts of Aβ and Tau proteins in the different regions. In this study, the PMOD software was used to analyze PET data and extract SUVR values. The Desikan-Killiany template was similarly set as the basis for the delineation of the brain regions, and the average SUVR value for each region was calculated [22–24].

2.6. Evaluation of the predictive capacity of classifications

The ROC curve (receiver operating characteristic curve) is an important tool for evaluating the performance of binary classification models. It intuitively displays the relation between the true positive rate (TPR) (sensitivity) and the false positive rate (FPR) (specificity) of the classifier. The AUC is a measure of the overall classification ability of the model; the larger the AUC value, the stronger the predictive ability of the model. The AUC value ranges from 0 to 1, with a value close to 1 indicating that the model performs very well, and a value close to 0 indicating that the model is poorly effective. The closer the AUC value is to 1, the better the model performance [25]. The above analysis was performed using SPSS Statistics v27. In the SPSS ROC analysis, we selected the "closest to the upper left corner" criterion to determine the optimal cutoff point. This criterion calculates the geometric distance from each point on the ROC curve to the upper-left corner (0, 1) using the formula $\sqrt{[(1\text{-sensitivity})^2 + (1\text{-specificity})^2]}$, selecting the point with the shortest distance as the optimal threshold. This method is one of SPSS's built-in standards, designed to maximize the overall performance of a diagnostic test. SPSS automatically outputs the optimal threshold calculated using the above criterion, along with its corresponding sensitivity and specificity, in the results table. The values we report are directly derived from this output. To mitigate the influence of age, gender, and years of education on our results, we adjusted for these covariates. After controlling for these variables, the outcomes of the ROC analysis—

such as the AUC value—reflect the diagnostic capability of our model parameters independent of the aforementioned demographic factors.

3. Results

3.1. Model fitting

From the distribution states of the population-type 68 × 68 functional and structural connectivity matrices extracted from fMRI and DTI, respectively, as well as the FC matrices generated by the simulation, the highest correlation between the AD population empirical FCs and the simulated FCs was found to be 0.7. The correlation between empirical FCs and simulated FCs improved significantly from 0.46 [26] to 0.7 (see Figure 3); however, better modeling and further program optimization are still possible.

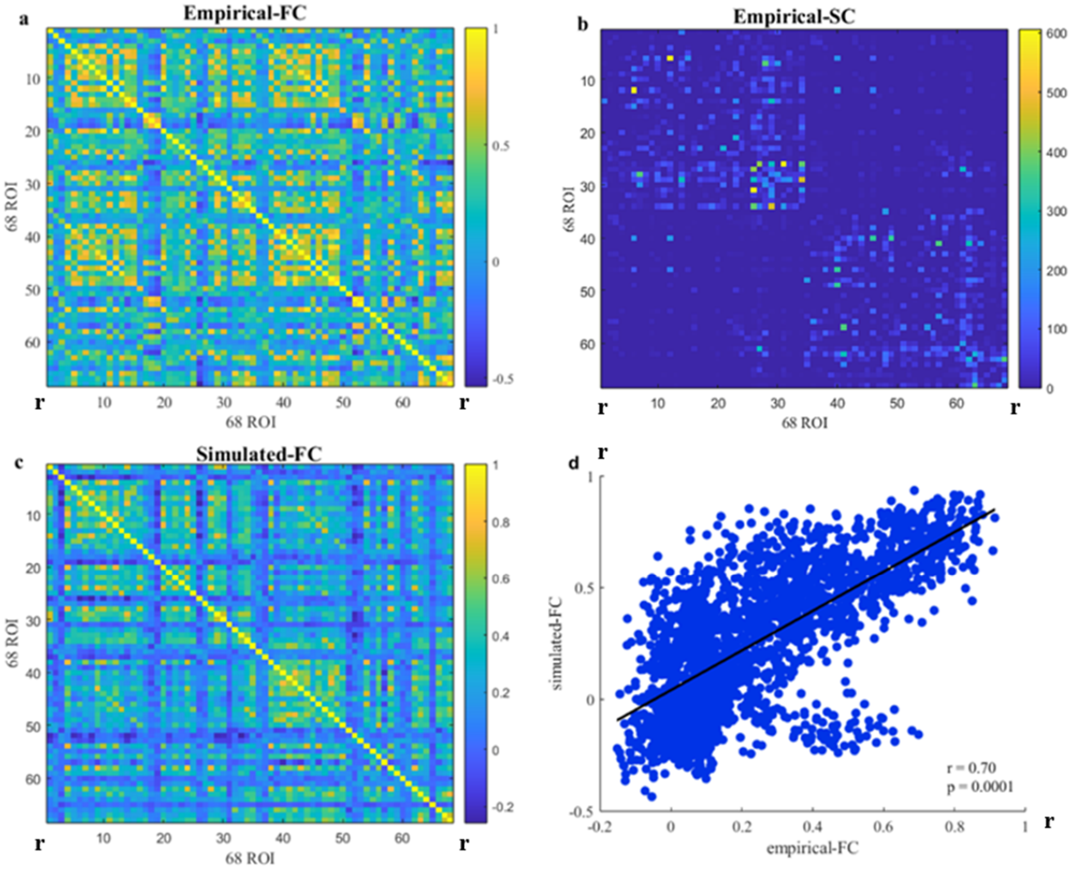

Figure 3. A better consistency between empirical and simulated FC is achieved by automatically optimizing the rMFM parameters. a) FC matrix of empirical AD obtained based on Desikan Killiany atlas. b) SC matrix of empirical AD obtained based on Desikan Killiany atlas. c) Simulated FC matrix obtained based on rMFM model simulation generation. d) Correlation between simulated FC and empirical FC.

Our results are similar to those of Honey et al. [26], who obtained SC from five healthy men by diffusion spectral imaging and simulated FC using a nonlinear neural mass model, and calculated the correlation between empirical and simulated FC, which was 0.70. Wang et al. [21] used the same model and data from the HCP database, and the correlation between empirical FC and simulated FC was only 0.46. The variability of the results did not allow for distinguishing between the ADNI and HCP databases, suggesting that the model may be more suitable for brain simulation of Alzheimer's disease.

3.2. Intergroup comparison of model parameters and dynamical results

3.2.1. Time-domain dynamics and spatial mapping analysis of neurovascular coupling

The preliminary results of the model include neural activity, cerebral blood flow (CBF) response, and BOLD signal changes in three groups of people: CN, EMCI, and AD, as shown in Figure 3. The resting state of the CBF value is set to 1, and the change in CBF under neural stimulation is obtained. Figure 3 shows that only certain brain regions exhibit slight differences in the trends of the three indicators, but the overall trends are consistent.

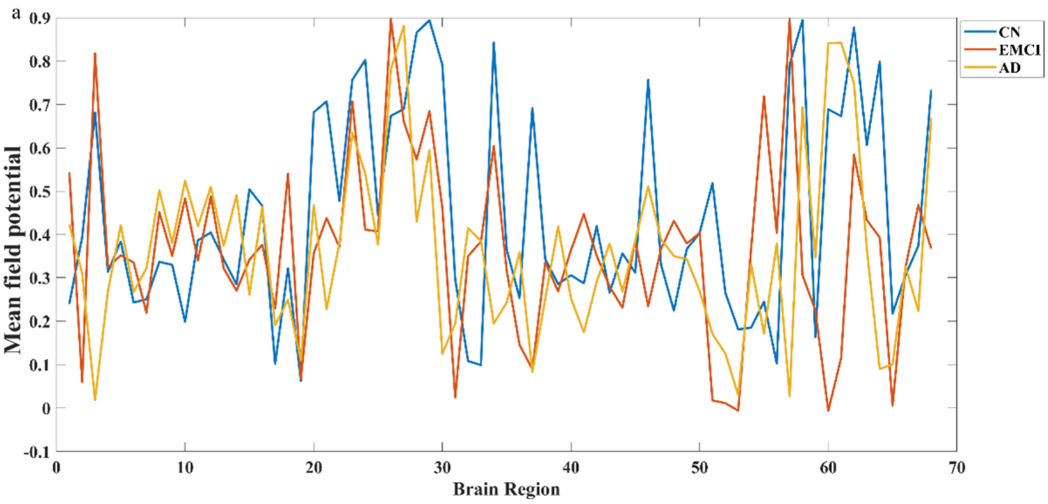

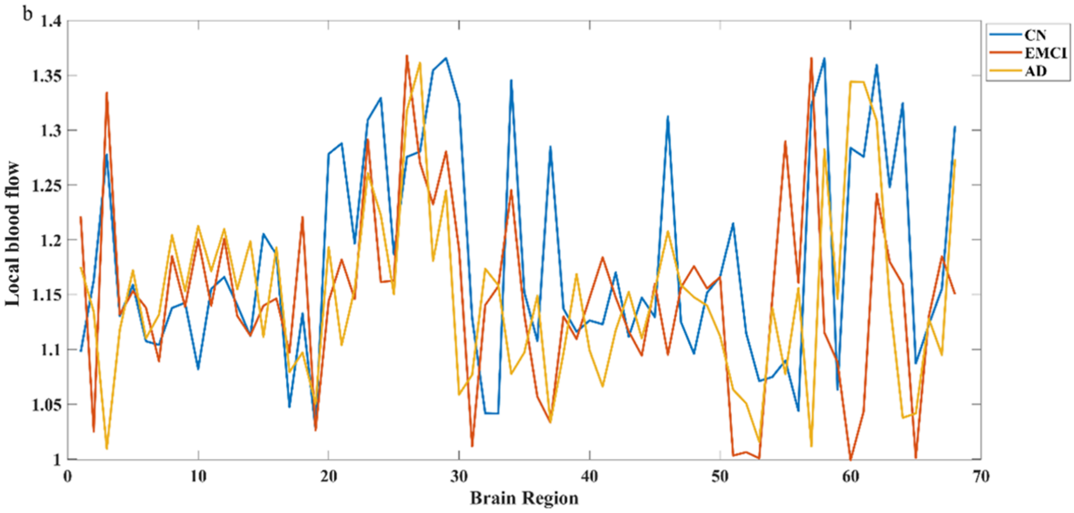

Continued on next page

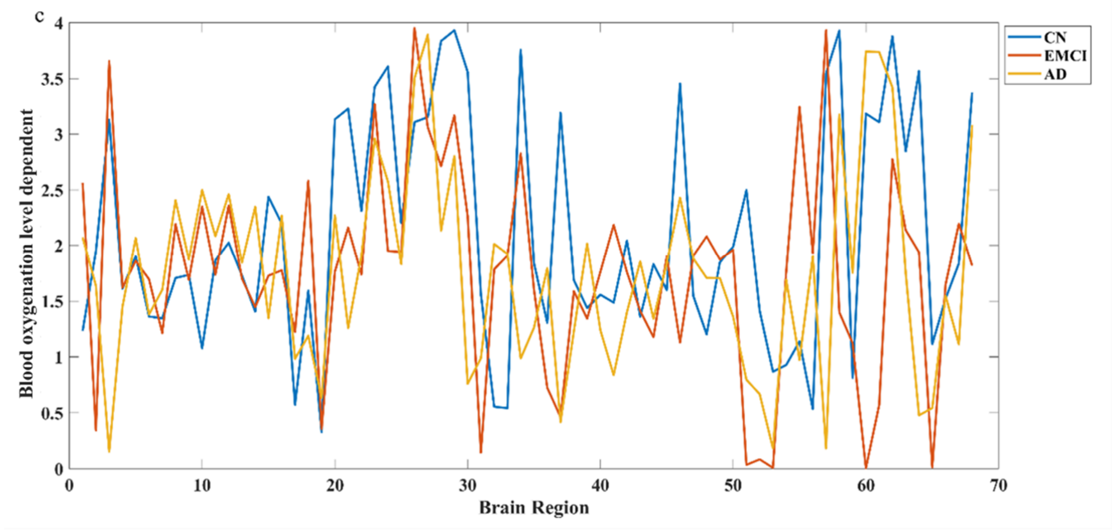

Figure 4. Neural activity (a), cerebral blood flow (CBF) response (b), and BOLD signal changes (c) in the CN, EMCI, and AD groups. The Y-axis in Figure 4a represents the mean synaptic gating variable of the excitatory neuronal population in the model, typically denoted as $<S_i>$.

Figure 5 shows the map of the average values of neural activity, cerebral blood flow, and BOLD signals in various regions of the brain of AD patients, to the surface of the brain layer, focusing on brain areas related to cognitive function.

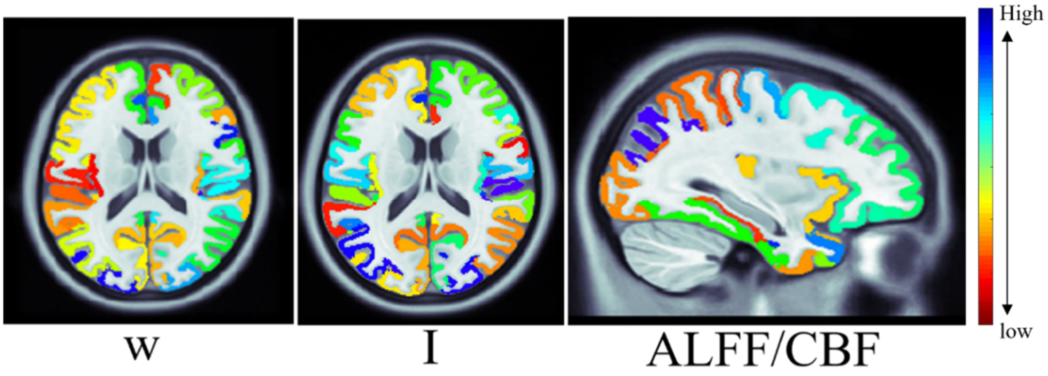

Figure 5. Schematic diagram of the average values of neural activity, cerebral blood flow, and BOLD signals in each brain region of the AD population.

3.2.2. Between-group comparison of model parameters and neuro-hemodynamics outputs

In this study, data were extracted from 118 ADNI participants (including CN, EMCI, and AD groups). Modeling yielded population-averaged w and I values, as well as simulated neuro-hemodynamics outputs including neural activity (see Eq (2.1) S_i), CBF, BOLD signal, and NVC parameters (ALFF/CBF); ALFF values characterized the degree of neurovascular coupling by the ratio of low-frequency amplitude calculated from the BOLD signal to the CBF. These comparison results are shown in Table 1. In the three group comparisons, the differences in neural activity, CBF, BOLD, and ALFF/CBF values were statistically significant (see Figure 6).

Table 1. Results of comparison of differences in parameters.

	CN (n = 42)	EMCI (n = 38)	AD (n = 38)	P-value
w	0.54 (0.11)	0.55 (0.13)	0.55 (0.17)	0.8122
I	0.32 (0.06)	0.38 (0.15)	0.35 (0.14)	0.0208*
Neural activity	0.45 (0.22)	0.46 (0.22)	0.59 (0.26)	0.0014*
CBF	1.19 (0.09)	1.19 (0.1)	1.24 (0.11)	0.0016*
BOLD	2.16 (0.93)	2.19 (1.07)	2.71 (1.13)	0.0029*
ALFF/CBF	0.6 (0.19)	0.61 (0.21)	0.7 (0.24)	1.13e-15*

The value represents the mean of the corresponding indicator in the population, the value in parentheses indicates the standard deviation of the corresponding data, and the p-value was obtained using analysis of variance (ANOVA) to test differences among the three groups. * Indicates statistically significant differences ($p < 0.05$).

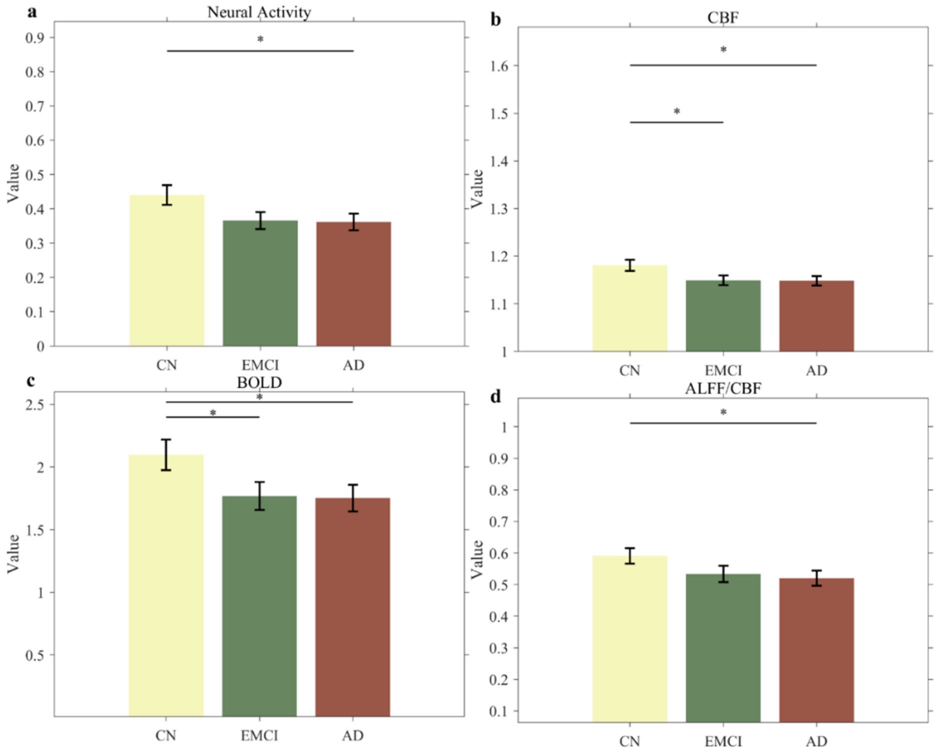

Figure 6. Results of statistical analysis of differences in parametric dynamical parameters for the three cohorts. (a) Box plots of the intensity of synaptic activity in the three groups of CN, EMCI, and AD; differences between CN and AD. (b) Box plots of the CBF in the three groups of CN, EMCI, and AD; differences between CN and EMCI, and between CN and AD. (c) Box plots of the BOLD signal in the three groups of CN, EMCI, and AD; differences between CN and EMCI, and between CN and AD. (d) Box plots of ALFF/CBF for the three groups of CN, EMCI, and AD; difference between CN and AD. ***$p < 0.001$,**$0.001 < p < 0.01$,*$0.01 < p < 0.05$).

3.2.3. Results of SUVR value and comparison between groups

In the whole brain range, SUVR values were extracted from PET scans of CN, EMCI, and AD, and the results are shown in Table 2, with statistically significant differences in both Aβ and Tau comparisons. The differences in Aβ were statistically significant between the CN and AD groups, and between the EMCI and AD groups ($P < 0.01$), and the differences in Tau between the CN and EMCI groups, and between the EMCI and AD groups, were statistically significant ($P < 0.01$ and $P = 0.0024$) (see Figure 7).

Table 2. Comparative results of differences in SUVR values for Aβ and Tau.

	CN (n = 42)	EMCI (n = 38)	AD (n = 38)	P value
Aβ	0.79 (0.04)	0.79 (0.04)	0.85 (0.05)	5.63e-15*
Tau	0.78 (0.04)	0.81 (0.04)	0.75 (0.16)	0.0013*

Values indicate the mean of SUVR in the group, values in parentheses indicate the standard deviation of the corresponding data, and p-values represent the significance of the differences between the three groups obtained by ANOVA. * Indicates statistically significant differences ($p < 0.05$).

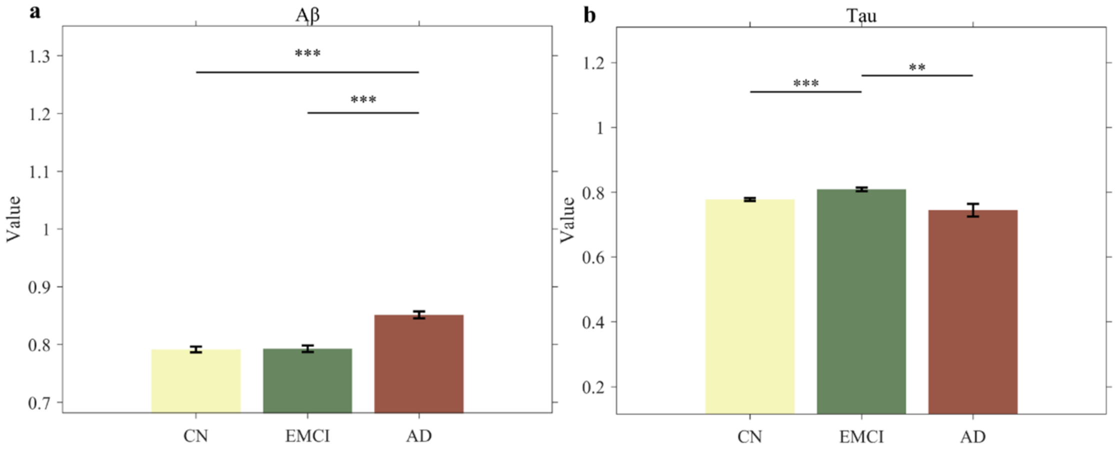

Figure 7. Comparison of differences between Aβ and Tau groups, with SUVR values in vertical coordinates. (a) Box plots of the differences in the extent of Aβ protein deposition in the CN, EMCI, and AD groups; differences between EMCI and AD, and between CN and AD. (b) Box plots of the differences in the extent of Tau protein deposition in the CN, EMCI, and AD groups; differences between CN and EMCI, and between EMCI and AD.

3.2.4. Correlation analysis between model parameters, neurovascular coupling parameters, and protein content

In this section, the results of Pearson correlation analysis from 118 cases (Table 3) showed that w was positively correlated with Tau ($r = 0.1564$, $P = 0.0255$); additionally, ALFF/CBF was positively correlated with Aβ ($r = 0.166$, $P = 0.0177$) and negatively correlated with Tau ($r = -0.1628$, $P = 0.02$) (see Figure 8).

Table 3. Results of Pearson correlation analysis between model parameters, NVC parameters, and protein content.

	w		I		ALFF/CBF	
	r	P-value	r	P-value	r	P-value
Aβ	0.1108	0.1148	0.0693	0.3250	0.166	0.0177*
Tau	0.1564	0.0255*	0.0277	0.6936	-0.1628	0.0200*

*Indicates statistically significant differences ($p < 0.05$).

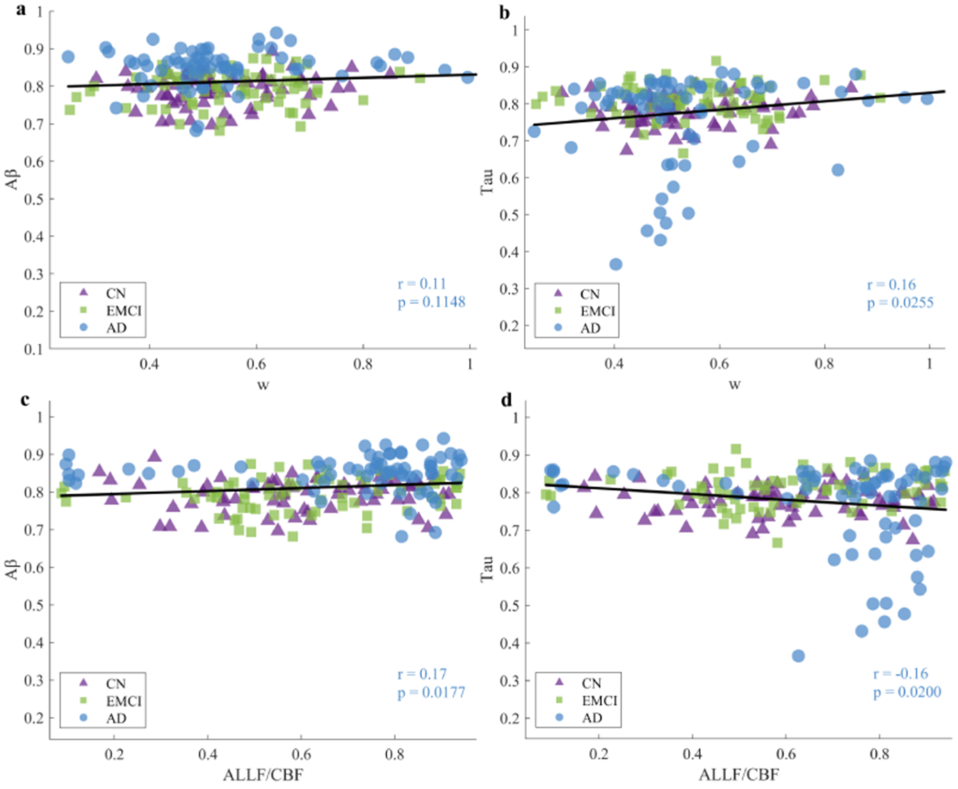

Figure 8. (a) Scatterplots of w and Aβ in the CN, EMCI, and AD groups show that w is not related to Aβ, whereas (b) w and Tau are significantly positively correlated in the EMCI and AD groups. (c) Scatterplots of ALFF/CBF and Aβ in the CN, EMCI, and AD groups show a positive correlation, and (d) scatterplots of ALFF/CBF and Tau in the CN, EMCI, and AD groups show a negative correlation. CN is the blue dot, EMCI is the red dot, and AD is the green dot.

3.3. Performance evaluation of model parameters and neurovascular coupling parameters in AD diagnosis

In order to investigate the role of w, I, and NVC index ALFF/CBF in the diagnosis of CN and EMCI, we assessed the predictive outcomes of those parameters used to distinguish between the two populations by plotting ROC curves. Results (Figure 9(a) and Table 4) showed that, after correcting for the covariates (age, sex, and years of education), the w, I, and neurovascular coupling index ALFF/CBF were 0.74, 0.636, and 0.792, respectively. w had a cutoff value of 0.54139, high specificity (100%), and low sensitivity (46%). ALFF/CBF had a cutoff value of 0.34868, high sensitivity (91%), and low specificity (57%). Similarly, the ROCs of the three indices were plotted between the CN and AD work characterization curves, and the results (Figure 9(b) and Table 5) showed that after correction for covariates, the AUC values of w, I, and the neurovascular coupling index ALFF/CBF used to discriminate between the two populations were 0.49, 0.84, and 0.56, respectively, with a critical point of I (0.54139), which is high in sensitivity and low in specificity.

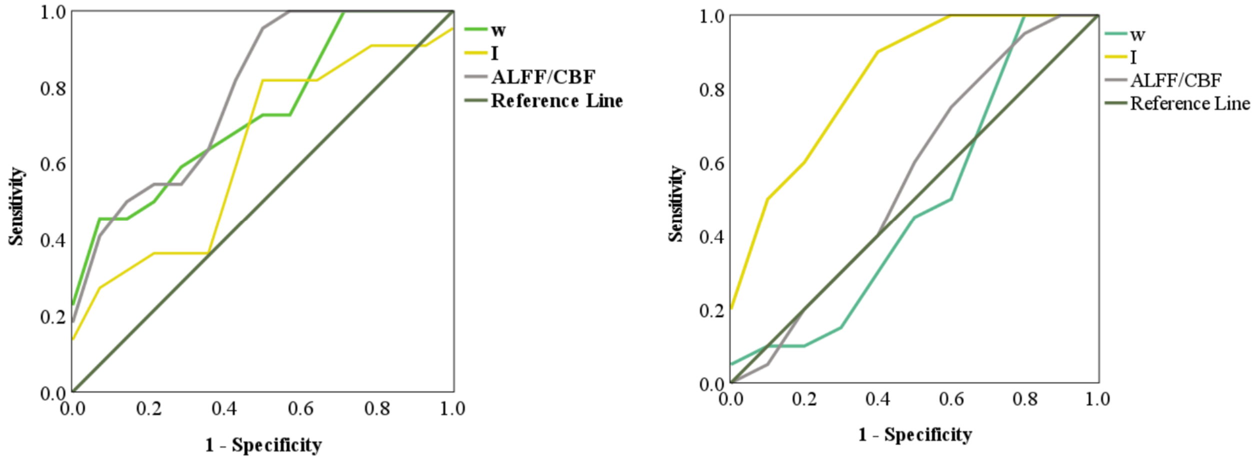

(a) (b)

Figure 9. (a) Subject working characteristic curves based on potential predictors in the discrimination between CN and EMCI. (b) Subject working characteristic curves based on potential predictors in the discrimination between CN and AD.

Table 4. w, I, and ALFF/CBF indicators for distinguishing between CN and EMCI predictions.

	AUC	Significance	95% CI	Intercept	Specificity	Sensitivity
w	0.740	<0.05	0.54–0.94	0.54139	100%	46%
I	0.636	0.25	0.407–0.868	–	–	–
ALFF/CBF	0.792	<0.05	0.617–0.968	0.34868	57%	91%

Table 5. w, I, and ALFF/CBF indicators for distinguishing between CN and AD predictions.

	AUC	Significance	95% CI	Intercept	Specificity	Sensitivity
W	0.490	0.94	0.22–0.76	0.502	30%	100%
I	0.840	<0.05	0.666–1	0.3202	30%	100%
ALFF/CBF	0.560	0.65	0.298–0.822	0.3165	50%	70%

– Represents an invalid value.

4. Discussion

4.1. Parameter estimation and pathological interpretation of dynamical results

In this study, we innovatively integrated fMRI and DTI multimodal imaging data, combined mean-field modeling with hemodynamic modeling, and constructed a whole-brain neurovascular coupling computational framework with clinical practical value. The modeling method has the following advantages:

1) Adoption of noninvasive and low-radiation imaging technology, which is suitable for long-term follow-up monitoring.

2) Individualized parameter estimation through mathematical modeling, which significantly improves diagnostic sensitivity.

3) Providing a quantitative assessment tool for early intervention.

Intergroup analysis revealed that CBF and BOLD signals were significantly different between CN and EMCI groups ($p < 0.01$); the ALFF/CBF ratio showed a monotonically decreasing trend in the course of disease progression; parameter abnormality in the EMCI stage suggests early neurovascular unit dysfunction; and deterioration of parameters in the AD stage reflects reduced synaptic function and vasoregulatory ability in the late stage of the disease, implying a neurometabolic vascular unit dysfunction and a decline in vascular regulation, which implies an imbalance in neurometabolic–blood flow coupling. These findings provide dynamic and quantitative indicators for understanding AD progression.

The results of this study indicate that tau pathology and neurovascular coupling (NVC) parameters, such as ALFF and CBF, exhibit significant nonlinear synergistic changes during disease progression. During the ECMI stage, accompanied by substantial accumulation of tau pathology, both ALFF and CBF exhibit synchronous elevation or remain at elevated levels. This may reflect the brain’s intrinsic mechanism of compensating for neuronal damage and clearing toxic substances by enhancing blood flow and metabolic activity. Upon progression to the AD stage, as pathology exceeds a critical threshold, neurovascular units undergo decompensation, leading to a marked decline in both CBF and ALFF. This suggests a complete collapse of vascular regulatory mechanisms. This finding offers a crucial perspective on understanding AD progression: EMCI can be regarded as a critical compensatory window period. During this stage, neurovascular function retains compensatory potential, and NVC parameters may serve as biomarkers for assessing compensatory capacity. Abnormally elevated NVC values may signal the risk of compensatory mechanisms becoming overloaded and rapidly deteriorating. Therefore, interventions during the EMCI stage should not only target tau pathology but also prioritize protecting and enhancing neurovascular function—such as through vascular risk management or NVC-targeted therapies—to prolong the compensatory phase and delay disease progression.

The consistency between simulated neural activity (the average synaptic gating variable $<S_i>$) and the BOLD signal directly embodies the physiological neurovascular coupling (NVC) phenomenon captured by our model. This coupling refers to the mechanism where increased neuronal activity triggers local vasodilation and elevated blood flow (the hemodynamic response), which in turn generates a measurable BOLD signal. The temporal synchrony of their trends—such as reaching peak values simultaneously—indicates that our model successfully reproduces one of the brain's most fundamental physiological mechanisms. Consistency provides robust qualitative validation of the model’s validity, demonstrating that our model is not only mathematically stable but also generates outputs consistent with biological logic. This validates the correctness of the model's core architecture—particularly the soundness of the entire forward generative process from neural activity to hemodynamic response. We acknowledge that this primarily falls within the realm of qualitative validation. While rigorous quantitative accuracy metrics (such as the coefficient of determination R^2) remain unquantified, this validation demonstrates the model's capability to generate expected patterns.

More rigorous quantitative validation requires direct comparison and parameter fitting based on refined experimental data—such as synchronously recorded local brain potentials and BOLD functional MRI signals—which will be a key focus of our future work.

4.2. Significant differences in protein content between groups

Aβ protein showed progressive accumulation: CN vs. EMCI vs. AD groups (P = 5.63e-15) and a linear growth pattern in line with the "amyloid cascade" hypothesis. Tau protein showed nonlinear changes, with a significant difference between the groups (P = 0.0013). Peak accumulation in the EMCI group suggests that its molecular characterization acts as a key stage of disease transformation. Clinically, the persistent deposition of Aβ may trigger synaptotoxic effects and disruption of the blood–brain barrier, and the aberrant phosphorylation of Tau leads to disintegration of the microtubule system, impaired axonal transport, and even direct impairment of synaptic plasticity.

4.3. Parameter and protein correlation results combined with physiological process interpretation

Aβ proteins (β-amyloid precursor proteins) and Tau proteins (Tau proteins) are among the most important biomarkers of AD, and understanding their role in disease progression is critical for the discovery of new therapeutic strategies and early interventions. The neurovascular coupling (NVC) metric proposed in this paper is based on resting-state functional magnetic resonance imaging (rs-fMRI). It is completely non-invasive and radiation-free, enabling repeatable, dynamic, and region-specific assessment of brain functional states. Compared to cerebrospinal fluid testing requiring lumbar puncture or Aβ-PET imaging involving radiation exposure risks, this method is more suitable for population screening, long-term follow-up, and clinical trials requiring frequent monitoring. The NVC metric is not intended to replace molecular biomarkers such as Aβ or Tau, but rather serves as a complementary functional assessment tool, offering new insights into understanding the pathological mechanisms of Alzheimer's disease and evaluating the efficacy of therapeutic interventions.

4.3.1. Pearson correlation results

In this study, we investigated the relationship between brain connectivity strength (w), ALFF/CBF, and AD-related proteins Tau and Aβ. The results showed that w was positively correlated with Tau, and ALFF/CBF was positively correlated with Aβ and negatively correlated with Tau. w elevation may be a risk factor for AD, and ALFF/CBF elevation may be a protective factor and serve as a biomarker for the diagnosis of AD and prediction of EMCI transformation. Due to the complex pathogenesis of AD, the accumulation of Aβ and Tau, although an influential factor, is not the only pathogenesis. Other factors, such as inflammatory response, vascular dysfunction, and iron dysregulation, may affect both neural and blood flow. In the early stages of pathogenesis, the accumulation of Aβ may not yet have caused significant blood flow changes or functional alterations, and thus, the correlation is low, whereas in the complex brain, localized cerebral blood flow changes may then be averaged out by the model, thus affecting the overall estimation. Thus, the correlations between w, ALFF/CBF, and the content of the two proteins, significant but lower, are reasonable.

4.3.2. Finding indicator thresholds and sensitivity-specificity judgments

According to the ROC curve results, the critical value of w has a high specificity (100%) and hardly misdiagnoses healthy individuals, but it has a low sensitivity (46%) and may miss many patients, making it insufficiently sensitive as a screening tool alone. In contrast, ALFF/CBF has a high critical value sensitivity (91%), which identifies most patients, but a low specificity (57%), which may lead to misdiagnosis in healthy individuals. Combining the two metric balances sensitivity and specificity: high-risk individuals are first screened using the highly sensitive ALFF/CBF (sensitivity 91%, specificity 57%) to ensure that potential patients are not missed; although false positives may exist, they can be ruled out by subsequent accurate testing. A confirmatory diagnosis is then made using the highly specific w (specificity 100%, sensitivity 46%) to reduce the risk of misdiagnosis. This dual screening strategy improves the accuracy of early screening for AD through categorization and result fusion for different clinical stages and patient populations. The clinical amyloid PET misdiagnosis rate can be as high as 10%–40%, and we re-selected 41 CN and EMCIs with the same condition, with 39 meeting our threshold range, meaning that our correctness rate was superior to the clinical test results. Combining w and ALFF/CBF can balance sensitivity and specificity, suggesting that the two can be used as potential biomarkers for early diagnosis of AD, providing new ideas for disease prevention and diagnosis.

4.4. Limitations

This modeling scale is too large, ignoring the link between the interaction between excitatory and inhibitory neurons and disease progression. Although the world’s largest database (ADNI) was chosen, the small amount of data selected led to a lack of confidence in the results. There is a need for a deeper exploration of how multiple factors, such as neuroinflammation, metabolic abnormalities, and genetic susceptibility, work together to trigger and accelerate the onset and progression of disease. The simplified structure of current models imposes certain limitations on their performance. For instance, they fail to adequately simulate the heterogeneous global coupling mechanisms within brain networks (such as white matter fiber-specific connections) and typically assume homogeneity among neuronal populations, overlooking differences in cell types and microstructures across brain regions. Regarding parameter estimation, the model faces challenges of overfitting and underconstraint. Global parameterization strategies struggle to capture the intrinsic dynamics of distinct neural circuits, potentially yielding non-unique or suboptimal solutions. Furthermore, relying on static functional connectivity as the fitting target sacrifices crucial temporal dynamics, while noise in fMRI data and preprocessing workflows introduces systematic biases. To enhance model accuracy, future work may incorporate hierarchical Bayesian frameworks and more complex node dynamics models. Adopting multi-objective optimization and dynamic functional connectivity metrics as fitting targets, while integrating individualized structural connectivity with task-state fMRI data, could strengthen the model's biophysical plausibility and its ability to capture spatiotemporal dynamics. Although this study mitigated the risk of overfitting to some extent through group validation and parameter constraints, we recognize that future work should employ more sophisticated regularization techniques (such as L2 regularization) to further enhance the model’s generalization capability and strengthen the stability of parameter estimation. Furthermore, incorporating E/I balance into the model will significantly enhance its ability to capture the complexity of neurovascular dysfunction in AD; on one hand, it exacerbates pathology and disrupts blood flow regulation by amplifying abnormal neural activity; on the other hand, it catalyzes an energy crisis due to mismatched energy supply and demand, ultimately leading to brain network dysfunction and cognitive decline.

5. Conclusions

In conclusion, we have conducted a comprehensive study of the different stages of AD and CN according to a whole-brain model suitable for CN. In addition to reproducing the neurological and hemodynamic studies of the different stages from CN to AD, our study demonstrated the ability of the model's indicators to predict early AD, proposed a dual detection strategy suitable for clinically differentiating between the CN and EMCI stages, and provided a new way of thinking about biomarker research for this disease. Thus, it can help improve the predictive ability of new indicators and discover new therapeutic directions.

Use of AI tools declaration

The authors declare they have not used Artificial Intelligence (AI) tools in the creation of this article.

Acknowledgments

This study was supported by the National Key Research and Development Program of China (Grant Nos. 2021YFA1000200 and 2021YFA1000202) and the National Natural Science Foundation of China (Grant Nos. 12572064, 12102014, 32271361 and 12202022).

Conflict of interest

The authors declare there is no conflict of interest.

References

1. K. Kisler, A. R. Nelson, A. Montagne, B. V. Zlokovic, Cerebral blood flow regulation and neurovascular dysfunction in Alzheimer disease, *Nat. Rev. Neurosci.*, **18** (2017), 419–434. https://doi.org/10.1038/nrn.2017.48
2. J. Wang, X. Yang, Dynamic modeling of astrocyte-neuron interactions under the influence of Aβ deposition, *Cognit. Neurodyn.*, **19** (2025), 60. https://doi.org/10.1007/s11571-025-10246-w
3. X. Ren, Y. Wang, X. Li, X. Wang, Z. Liu, J. Yang, et al., Attenuated heterogeneity of hippocampal neuron subsets in response to novelty induced by amyloid-β, *Cognit. Neurodyn.*, **19** (2025), 56. https://doi.org/10.1007/s11571-025-10237-x
4. Z. Yang, F. Lange, Y. Xia, C. Chertavian, K. Cabolis, M. Sajic, et al., Nimodipine protects vascular and cognitive function in an animal model of cerebral small vessel disease, *Stroke*, **55** (2024), 1914–1922. https://doi.org/10.1161/STROKEAHA.124.047154
5. A. R. Bateman, J. Lechner-Scott, T. Barber, G. A. Bateman, S. Ramadan, R. Lea, A longitudinal investigation of the cerebral venous hemodynamics in multiple sclerosis using computational fluid dynamics, *Multiple Scler. Relat. Disord.*, **100** (2025), 106555. https://doi.org/10.1016/j.msard.2025.106555

6. X. Chen, S. Li, Expert consensus on the application of amyloid-PET imaging in the diagnosis of Alzheimer's disease, *National Med. J. China*, **103** (2023), 3615–3626. https://doi.org/10.3760/cma.j.cn112137-20230909-00433
7. S. G. Mueller, M. W. Weiner, L. J. Thal, C. R. Jack, W. J. Jagust, J. Q. Trojanowski, et al., The Alzheimer's disease neuroimaging initiative, *Neuroimaging Clin. N. Am.*, **15** (2005), 869–877. https://doi.org/10.1016/j.nic.2005.09.008
8. L. Stefanovski, J. M. Meier, R. K. Pai, P. Triebkorn, T. Lett, L. Martin, et al., Bridging scales in Alzheimer's disease: Biological framework for brain simulation with The Virtual Brain, *Front. Neuroinform.*, **15** (2021), 630172. https://doi.org/10.3389/fninf.2021.630172
9. C. R. Jack Jr, D. A. Bennett, K. Blennow, M. C. Carrillo, B. Dunn, S. B. Haeberlein, et al., NIA-AA research framework: toward a biological definition of Alzheimer's disease, *J. Alzheimers Assoc.*, **14** (2018), 535–562. https://doi.org/10.1016/j.jalz.2018.02.018
10. G. McKhann, D. Drachman, M. Folstein, R. Katzman, D. Price, E. M. Stadlan, Clinical diagnosis of Alzheimer's disease: Report of the NINCDS—ADRDA work group under the auspices of Department of Health and Human Services Task Force on Alzheimer's disease, *Neurology*, **77** (2011), 333. https://doi.org/10.1212/01.wnl.0000400650.92875.cf
11. F. C. Yeh, I. M. Zaydan, V. R. Suski, D. Lacomis, R. M. Richardson, J. C. Maroon, et al., Differential tractography as a track-based biomarker for neuronal injury, *NeuroImage*, **202** (2019), 116131. https://doi.org/10.1016/j.neuroimage.2019.116131
12. F. C. Yeh, T. D. Verstynen, Y. Wang, J. C. Fernández-Miranda, W. I. Tseng, Deterministic diffusion fiber tracking improved by quantitative anisotropy, *PLoS One*, **9** (2014). https://doi.org/10.1371/annotation/0f3b12de-8b8b-4dda-9ff4-835b8631e1dc
13. F. C. Yeh, V. J. Wedeen, W. I. Tseng, Generalized q-sampling imaging, *IEEE Trans. Med. Imaging*, **29** (2010), 1626–1635. https://doi.org/10.1109/TMI.2010.2045126
14. F. C. Yeh, P. F. Tang, W. I. Tseng, Diffusion MRI connectometry automatically reveals affected fiber pathways in individuals with chronic stroke, *NeuroImage Clin.*, **2** (2013), 912–921. https://doi.org/10.1016/j.nicl.2013.06.014
15. X. Z. Jia, J. Wang, H. Y. Sun, H. Zhang, W. Liao, Z. Wang, et al., RESTplus: an improved toolkit for resting-state functional magnetic resonance imaging data processing, *Sci. Bull.*, **64** (2019), 953–954. https://doi.org/10.1016/j.scib.2019.05.008
16. H. M. Lin, Y. H. Yang, J. Y. Lu, Z. W. Zhang, S. F. Chen, J. J. Ge, et al. Visualization of brain abnormal β-amyloid deposition in Alzheimer's disease based on 18F-Florbetaben PET imaging, *Chin. J. Med. Imaging*, **32** (2024), 420–425. https://doi.org/10.3969/j.issn.1005-5185.2024.05.002
17. G. Deco, A. Ponce-Alvarez, D. Mantini, G. L. Romani, P. Hagmann, M. Corbetta, Resting-state functional connectivity emerges from structurally and dynamically shaped slow linear fluctuations, *J. Neurosci.*, **33** (2013), 11239–11252. https://doi.org/10.1523/JNEUROSCI.1091-13.2013
18. K. J. Friston, L. Harrison, W. Penny, Dynamic causal modelling, *NeuroImage*, **19** (2003), 1273–1302. https://doi.org/10.1016/S1053-8119(03)00202-7
19. K. E. Stephan, N. Weiskopf, P. M. Drysdale, P. A. Robinson, K. J. Friston, et al., Comparing hemodynamic models with DCM, *NeuroImage*, **38** (2007), 387–401. https://doi.org/10.1016/j.neuroimage.2007.07.040

20. J. Heinzle, P. J. Koopmans, H. E. M. den Ouden, S. Raman, K. E. Stephan, A hemodynamic model for layered bold signals, *NeuroImage*, **125** (2016), 556–570. https://doi.org/10.1016/j.neuroimage.2015.10.025
21. P. Wang, T. R. Knösche, A realistic neural mass model of the cortex with laminar-specific connections and synaptic plasticity—evaluation with auditory habituation, *PLoS One*, **8** (2013). https://doi.org/10.1371/journal.pone.0077876
22. P. Honhar, D. Matuskey, R. E. Carson, A. T. Hillmer, Improving SUVR quantification by correcting for Radiotracer clearance in tissue, *J. Cereb. Blood Flow Metab.*, **44** (2023), 296–309. https://doi.org/10.1177/0271678X231196804
23. J. Soucy, F. Mohammadi, T. Boulier, V. Hortelan, P. Rosa-Neto, T. A. Pascoal, et al., Different relationship of cross-regional correlations of progression of local cortical thickness and local SUVR 18f-flortaucipir PET values to strength of connectivity, *J. Alzheimers Assoc.*, **16** (2020), e037267. https://doi.org/10.1002/alz.037267
24. K. R. Thomas, A. J. Weigand, L. C. Edwards, E. C. Edmonds, K. J. Bangen, G. Ortiz, et al., Tau levels are higher in objective subtle cognitive decline but not subjective memory complaint, *Alzheimers Res. Ther.*, **14** (2022), 114. https://doi.org/10.1186/s13195-022-01060-1
25. C. E. Metz, Some practical issues of experimental design and data analysis in Radiological Roc Studies, *Invest. Radiol.*, **24** (1989), 234–245. https://doi.org/10.1097/00004424-198903000-00012
26. C. J. Honey, O. Sporns, L. Cammoun, X. Gigandet, J. P. Thiran, R. Meuli, et al., Predicting human resting-state functional connectivity from structural connectivity, *Proc. Natl. Acad. Sci. U.S.A.*, **106** (2009), 2035–2040. https://doi.org/10.1073/pnas.0811168106

AIMS Press